Journal of Molecular Liquids 438 (2025) 128602

Contents lists available at ScienceDirect

Journal of Molecular Liquids

journal homepage: www.elsevier.com/locate/molliq

Temperature-dependent structural evolution from order to disorder in sapphire-supported imidazolium ionic liquid films

Kevin Höllring [a], Nataša Vučemilović-Alagić [b,a], David M. Smith [b], Ana-Sunčana Smith [a,b,*]

[a] PULS Group, Institute for Theoretical Physics, FAU Erlangen-Nürnberg, Cauerstraße 3, 91058, Erlangen, Germany
[b] Group of Computational Life Sciences, Department of Physical Chemistry, Ruđer Bošković Institute, Bijenička 54, Zagreb, 10000, Croatia

HIGHLIGHTS

- When wetting a surface, liquids can form monolayers or bi-layers depending on surface-liquid and liquid-internal interaction forces.
- The competition between adhesion, cohesion and thermal excitation energies causes the film to undergo a solid-like to liquid-like transition.
- The transition impacts the frequency, size and shape of defects appearing in monolayers.
- We provide a new analysis technique to detect shape parameters of periodic monolayers and use it to investigate these shape changes.
- The surface saturation impacts the tendency to form monolayer or bi-layer structures and is a crucial factor during the initial wetting of a surface.

GRAPHICAL ABSTRACT

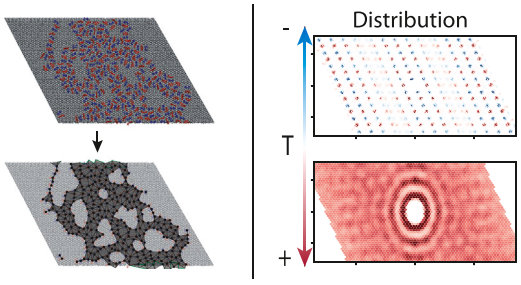

ARTICLE INFO

Keywords:
Wetting
Monolayer film
Ionic liquids
Phase change
Structural analysis
Molecular dynamics

ABSTRACT

Hypothesis: Imidazolium-based ionic liquids supported on alumina are central to various technological processes. We hypothesize that molecular interactions—both ion-ion and ion-surface—govern film structure and stability as a function of temperature and concentration.

Methods and simulations: We aim to optimize these systems through control of thermodynamic parameters in molecular dynamics simulations of 1,3-Dimethylimidazolium Bis-(trifluormethylsulfonyl)- imid ionic liquid monolayers spreading on hydroxylated alumina substrate at temperatures from 200 K to 400 K. We develop computational tools to analyze structural properties of molecular arrangement in the emergent monolayer, the structure of the film and the defects spontaneously forming and healing.

Findings: We find that the structure of the film is sensitive to temperature, with the appearance of a crystalline-like phase within the expanding film while the bulk IL is still deeply in the liquid phase. We furthermore show that surface coverage affects the level of order at low temperatures and the number of defects within the film at high temperatures. We relate these results to absolute and relative changes in cohesion energy between ions in the film and adhesion energy generated by hydrogen bonds with the surface.

* Corresponding author at: PULS Group, Institute for Theoretical Physics, FAU Erlangen-Nürnberg, Cauerstraße 3, 91058, Erlangen, Germany.
Email address: ana-suncana.smith@fau.de, asmith@irb.hr (A.-S. Smith).

https://doi.org/10.1016/j.molliq.2025.128602
Received 16 July 2025; Received in revised form 9 September 2025; Accepted 22 September 2025
Available online 24 September 2025

1. Introduction

The processes at the interface between ionic liquids (ILs), metals and their oxides are vital for technological progress in many fields of application including electrochemical deposition, nanoscale tribology, batteries, or supported ionic liquid phase catalysis [1] to name a few. The importance of the solid phase, whether functional or not, emerges due to the strong interfacial structuring of ILs, induced by adhesive forces, the intensity of which depends on the nature of the interactions between IL ions and the exposed surface layer of the support. Ultimately, these interactions determine the wetting behavior of the IL [2], the mobility of the ions and the reactants throughout the thin film [3,4], and may affect various technological processes.

The formation of IL films has been extensively studied on metal surfaces such as gold and platinum. For example, with regard to the wetting process of gold and platinum surfaces by 1,3-Dimethylimidazolium Bis-(trifluormethylsulfonyl)-imid ($[C_1C_1Im][NTf_2]$), characteristic changes in the monolayer structure could be measured depending on the degree of surface saturation [5] as well as depending on the temperature of the system [5,6]. At low temperatures with an unsaturated surface, the formation of islands of the IL film on the substrate was observed with overall hexagonal and occasionally striped crystalline patterns of the anion distribution. Further analysis showed that the crystalline-like phase can also be stabilized in an IL bilayer.

More recently, as a part of the development of alternatives to lithium-based batteries, there is a growing interest in exploring aluminium, as well as its oxide [7], which tends to form on the surface of the electrode [8], or can also be used as an inorganic, porous separator [9]. On neutral surfaces like fully hydroxylated alumina, IL adsorption is mainly governed by the formation of hydrogen bonds leading to a coupling between the liquid layer structure and the underlying substrate [2,10]. In films thicker than 10 nm, this leads to several, well-defined solvation shells propagating towards the bulk of the IL [2,11–15]. In thin films, it has been shown that the organization of the film depends on the film thickness, while the structure of the contact layer could be investigated in appreciable detail using a variety of experimental techniques [16–20]. However, unlike on gold, a precise analysis of the structural changes in these monolayers as a function of the thermodynamic conditions and the amount of IL deposited per unit surface area remains to be performed.

In this publication, we use molecular dynamics (MD) simulations as a tool to obtain quantitative information on the effects of temperature and surface saturation on the organization of 1-Ethyl-3-methylimidazolium Bis-(trifluor-methyl-sulfonyl)-imid ($[C_2Mim][NTf_2]$) deposited on a hydroxylated sapphire crystal, as a paradigmatic example of a system where full wetting is expected. By developing a tool to extract structural properties of the film, which may be useful beyond the current system, we demonstrate that temperature affects the balance between cohesive and adhesive forces acting between ions within the film, causing many-body correlations that may extend throughout the system, thereby defining mesoscopic morphological properties of the monolayer.

2. In-silico production of IL films

All simulations were performed using GROMACS 5.1.2 [21]. The ionic liquid (IL) consisted of $[C_2Mim]^+$ and $[NTf_2]^-$ ions. Parameters for the anion were adopted from the Canongia Lopes, Deschamps, and Padua (CLP) model [22], while for the cation, the parameters were taken from the well-established Maginn force field [23], which is an adaptation of CLP parameters using RESP charges to better capture dynamic and transport properties of IL. For the anion, further refinement of atomic charges was used as suggested in [2,3,24], which were derived using the RESP-HF method [25] at the HF/6-31 G(d) level of theory and scaled by a factor of 0.9. The sapphire was parameterized using the CLAYFF force field [26], fully hydroxylated using parameters available in the literature [13] and optimized with GULP [27]. Van der Waals interactions between the IL and the alumina surface were computed using the Lorentz-Berthelot mixing rules [2,13]. This force field combination accurately reproduces sapphire-IL X-ray reflectivity and IR spectroscopy data while preserving key bulk IL properties, such as average density, structure factor, and diffusion coefficients [2], and is particularly suitable for studying interfacial behavior of the chosen IL.

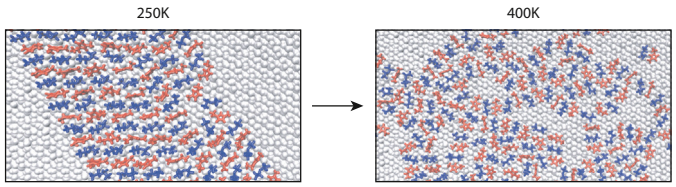

Fig. 1. Visualization of the characteristic molecular alignment and orientation below and above the critical temperature. Cations (red) and anions (blue) on top of the hydroxylated sapphire surface (silver) at 250 K are shown on the left and at 400 K on the right. The directional long-range order aligned with the sapphire crystal structure observed at low temperatures is lost at high temperatures, where only short-range order prevails reflected in an alternating anion/cation pattern. Furthermore, the formation of defects, seen as holes in the monolayer, is promoted at higher temperatures.

We systematically use a time step of 2 fs and a cut-off of 2 nm for the Van der Waals and short-range Coulomb interactions, while the Particle Mesh Ewald procedure was employed for the description of the long-range Coulomb interactions. All simulations were performed using periodic boundary conditions with a monoclinic geometry, as appropriate for the crystal's symmetry. Periodic copies of the slabs of alumina with the IL film were systematically separated by an 80 nm vacuum slab to eliminate long-range Coulomb forces that could affect the interface organization. The desired temperature was maintained with the Nosé-Hoover thermostat.

Monolayers were created starting from a 7.57 nm × 6.29 nm × 16 nm box of equilibrated IL consisting of 1800 pairs of $[C_2Mim]^+$ and $[NTf_2]^-$ ions. This IL was deposited on a sapphire substrate spanning 7.57 nm × 6.29 nm × 2.12 nm in xyz directions [3]. The combined system was re-equilibrated to the temperature of 300 K using semi-isotropic annealing along the z axis in NPT [2], followed by a 200 ns NVT run. After the thick film was equilibrated at 300 K, all but the first molecular layer of the IL film was removed. This resulted in 54 ion pairs on the sapphire surface which was, consequently, extended along the x-axis, to obtain a sapphire slab with an xy-dimension of 15.14×6.29 nm^2, and thus, a low level of surface saturation. The monolayer was then brought to and re-equilibrated at the desired temperature in an additional 100 ns run in the NVT-ensemble prior to a production run of 200 ns.

3. Wetting simulation and thermodynamic stability of the monolayer

To confirm that the monolayers are thermodynamically stable across the entire temperature range, we performed wetting simulations, which are a well-established approach for probing the interactions between ionic liquids (ILs) and solid substrates [28–30].

Each wetting simulation began with a fully equilibrated bulk liquid at the target temperature, prepared as described in the previous section. From this equilibrated box, we extracted cylindrical nanodroplets using VMD, with radii of r = 10 Å, 15 Å, and 22 Å. This geometry enables reliable averaging of the contact angle between the ionic liquid (IL) and the sapphire surface, Ojaghlou et al. [31] measured 46.5462 nm × 13.4364 nm × 2.12 nm in the x, y, and z directions, respectively. The droplet axis aligned with the (1000) crystal direction (see Fig. 2b), and wetting simulations were performed in the NVT ensemble. At 250 K,

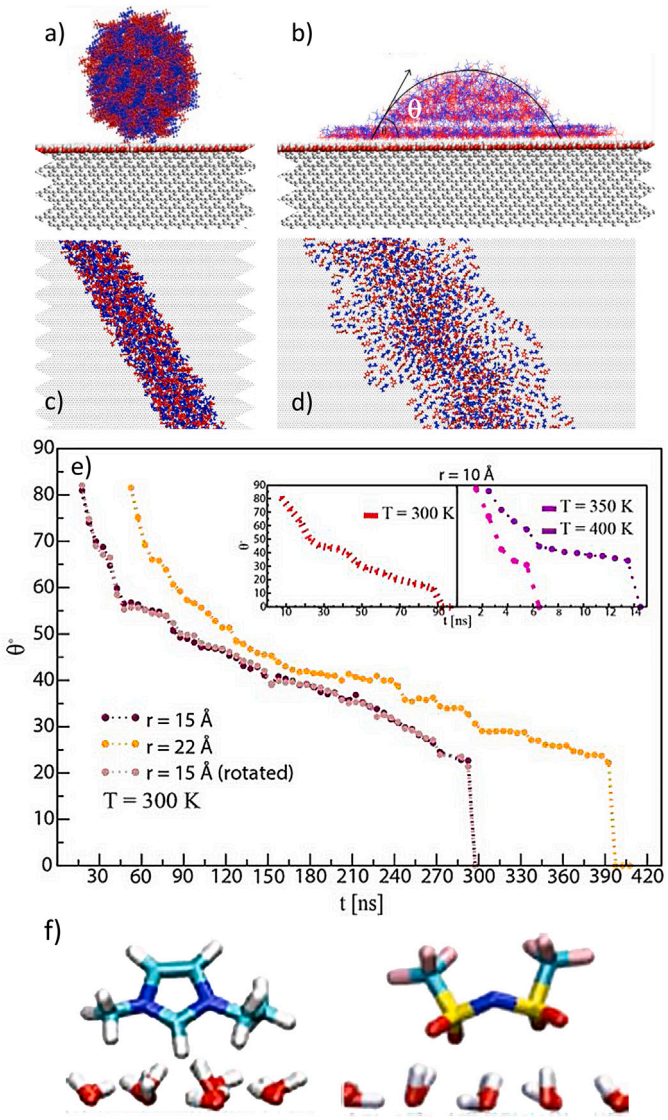

Fig. 2. Generating monolayers by complete wetting. IL nanodroplet in contact with the hydroxylated sapphire surface at the onset of the wetting simulations along the (1000) axis, shown from two perspectives: (a) along the axis and (b) over the *xy*-plane as in (c) and (d), respectively, during the spreading process which clearly progresses by the expansion of a precursor monolayer. (e) Effective spreading angle, shown in (c) as a function of time for nanodroplets of various sizes at 300 K, as well as at different temperatures (see insets). The curve annotated as "rotated" represents the spreading of a droplet initially aligned with the *y*-axis instead of a periodic axis of the crystal [24]. (f) Typical coordination of ions to the hydroxylated groups on the IL alumina to form hydrogen bonds.

the IL approached a glassy state, leading to dramatically slowed dynamics, such that spreading could not be observed even with the smallest droplets. At 300 K, 350 K, and 400 K, the duration of the production runs, extended until complete spreading was achieved, depended strongly on both droplet size and temperature, as shown in Fig. 2e (main panel and inset).

To examine whether the direction of spreading relative to the crystal lattice orientation affects wetting behavior, we exploited the cylindrical geometry of the droplet, which allows precise alignment along specific crystallographic axes. Using this setup, we compared spreading dynamics for a 15 Å nanodroplet at 300 K, initially aligned with the (1000) axis and rotated by 30° from it (aligned with the *y*-axis). As shown in Fig. 2e, we observed no measurable difference in wetting dynamics between these orientations, indicating that spreading occurs isotropically on the crystal surface.

All wetting simulations consistently demonstrate the formation of a precursor film during spreading (Fig. 2d). Contrary to the predictions of mesoscopic models for full wetting, which suggest that the thickness of the precursor film varies with distance from the droplet center [32], the precursor film formed by the current ionic liquid is a uniform monolayer. The monolayer is stabilized by strong cohesive Coulomb forces acting laterally within the film between ions of opposite charge and adhesive forces between the IL and the hydroxylated sapphire. The latter relies on cations using the hydrogen of the imidazole ring placed medially between the two nitrogens to form hydrogen bonds with the oxygens of the hydroxyl groups on the support. Meanwhile, the anion, predominantly in its cis-conformation, forms hydrogen bonds with its four oxygens pointing towards the surface (see Fig. 2f). These results are consistent with hydrogen bonds found at the interface of thick films of the same IL with the hydroxylated alumina [2,13].

The expansion of the monolayer during wetting is limited by the need to break hydrogen bonds, allowing ions within the film to move outward under the pressure exerted by ions in the droplet. Due to strong cohesive coupling between cation–anion pairs, this outward diffusion is highly correlated and cooperative. The resulting spreading of the film—i.e., the coordinated motion of ions at the film edge and across all layers between the edge and the droplet—is significantly slower than the local reorientation of ions required to form new hydrogen bonds, even at elevated temperatures. As a result, spreading dynamics are not influenced by the underlying alumina crystal axis, which governs reorientation, but are instead highly sensitive to both droplet size and temperature.

Specifically, larger droplets exert greater internal pressure, accelerating film expansion initially. However, as ions transfer from the droplet to the film, the droplet shrinks and internal pressure decreases, causing a marked slowdown in spreading. This is reflected in the change in slope in the spreading curves shown in Fig. 2e. Larger droplets require hundreds of nanoseconds to form a full monolayer, whereas smaller droplets complete spreading within tens of nanoseconds at the same temperature. As temperature increases, hydrogen bonds become less stable and ion diffusion accelerates, leading to faster spreading. For instance, a 1 nm droplet spreads over approximately 90 ns at 300 K, 15 ns at 350 K, and just 6 ns at 450 K (see inset of Fig. 2e).

We conclude that strong IL–substrate interactions mediated by hydrogen bonds promote full spreading, as anticipated [2,3,24]. The impact of hydrogen bonds on the formation of a monolayer has also recently been reported on a graphite surface, where the hydrogen bond network led to the formation of a checkerboard pattern [33].

Besides providing insights into spreading dynamics, the results of wetting simulations allow for a direct comparison between the resulting films and those generated from a thick film using the protocol described in the previous section. The structural agreement between these independently prepared films confirms that the observed film morphology does not depend on the preparation method, thereby showing no need for additional IL layers for the stabilization of these extra-thin films, as for example on Au(111) surfaces at only 300 K [6].

Notably however, as the temperature increases, the integrity of the monolayer is affected, which points to a competition between adhesive forces with the substrate (hydrogen bonds) and the cohesive forces between ions of opposing charge, acting laterally within the film.

4. Interplay between cohesive and adhesive forces

To gain further insights into the relative energetics of the cohesive and adhesive forces, we calculate the potential of mean force (PMF) between an ion or an ion pair of the monolayer and the alumina. This was achieved by pulling away the center of mass (COM) of an ion pair (or an ion) from a fully equilibrated monolayer obtained in the previous sections, in a direction perpendicular to the surface of the monolayer, i.e., along the *z*-axis.

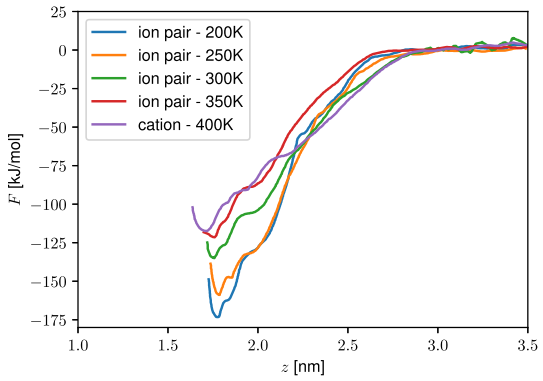

Fig. 3. Potential of Mean Force (PMF) at various temperatures. The PMF of an ion pair within the monolayer is shown for temperatures from 200 K to 400 K. At 400 K, the interaction potential is calculated exclusively for a cation. The adhesion energy is observed to drop as T is increased. (Figure as in the PhD thesis of an author [24].)

Sampling is achieved by first performing a 400 ps pull during which the COM is attached to a virtual particle (spring constant of 12,000 kJ mol^{-1} nm^{-2}) moving at a constant velocity of 0.01 nm ns^{-1}. From the obtained trajectory, we extract 16 configurations, wherein each successive configuration features the COM separated from the surface by an additional 0.01 nm along the z axis. At larger distances, 10 configurations are, furthermore, extracted for which the separation between successive COMs is increased to 0.1 nm. These 26 configurations are used for umbrella sampling, with a force constant of 5000 kJ mol^{-1} nm^{-2} applied to configurations distant from the surface, and 10 000 kJ mol^{-1} nm^{-2} for 16 configurations near the surface, in total covering separations of 1.85 nm from the positions within the monolayer. Each sampling configuration was propagated for 10 ns. Data from the first ns were omitted from the analysis. Convergence for all obtained distributions was checked by calculating PMFs for the first 8, 9 and 10 ns. The weighted histogram analysis method (WHAM) [34,35] was used to obtain unbiased PMFs. If we add up the simulation time over 26 windows, we obtain a total of 260 ns/PMF.

In our calculations of the potential of mean force (PMF) over the temperature range $200 < T < 400$ K, we consistently observed that pulling on a single ion inevitably resulted in the extraction of a cation–anion pair. This behavior occurred regardless of the applied force constant or pulling velocity, indicating that, within this regime, the adhesive interactions between an ion pair and the surface are weaker than the cohesive forces binding the ions together. To produce a comparable set of PMFs below 400 K, we therefore constrained the COM of a cation-anion pair. The corresponding PMFs, shown in Fig. 3, exhibit a pronounced minimum of approximately 180 kJ mol^{-1} at 200 K, which remains significant—around 130 kJ mol^{-1}—even at 400 K.

Only at 400 K were we able to extract a cation without simultaneously pulling its counterion. This marks the transition point at which the free energy of surface binding exceeds the cohesive energy of the ion pair. This behavior is captured in the PMF shown in Fig. 3, calculated by constraining only the center of mass of a single cation at 400 K. Notably, this PMF differs only slightly from those calculated for ion pairs, confirming that the observed effect arises from the loss of cohesive interactions rather than changes in surface adhesion. This finding is consistent with the breakdown of film integrity, with no appearance of any additional layers in the film under the investigated thermodynamic conditions.

5. The effects of temperature on the organization of IL monolayers

We now consider the average lateral distribution of ion pairs in the IL within the monolayer. From visual inspection of the trajectory alone, we observe a clear alternating pattern of cations and anions aligned with the (1000) axis of symmetry of the sapphire at low temperatures. This is contrasted by an isotropic, but still alternating pattern at higher temperatures (see Fig. 1), suggesting a transition from a crystalline-like to liquid-like behavior around room temperature. To quantify this heuristic observation, we extract the normalized relative density distribution in the xy-plane (2Drdf).

The 2Drdf (see Fig. 4) is obtained by calculating the spatial distribution of the COM position of all cations or anions relative to a cation, averaged over all possible initial cations and all frames in the production run (code and technical details available on https://github.com/puls-group/monolayer_analysis and [36]). Accordingly, the relative positions are binned on a two-dimensional hexagonal grid with dx and dy of ≈ 0.1 nm side length. Because the monolayer has the appearance of an infinite strip along the (1000) axis, we normalize the distribution along the x-axis using a rescaling factor of $\propto 1/(a - |dx|)$, where a denotes the finite width of the film in x-direction, which allows us to compare different axes. We furthermore, normalize the distributions to 1 at their maxima to allow for better visibility.

We find that at low temperatures (200 K to 300 K; top panels in Fig. 4), the relative distribution function reveals alternating cation–anion alignment, forming stripes of like-charged ions along the x-axis. This corresponds to two intercalated, distorted hexagonal lattices—one for each ion species. The structure is clearly aligned with the periodicity of the (0001) sapphire surface, driven by the distribution of hydroxyl groups and hydrogen bonding, which suppresses ion mobility. This is in contrast to [C_1Mim][NTf_2] on Au(111), where misalignment with the substrate was reported [6]. Together with Coulomb interactions and a nearly-complete suppression of diffusion, these effects promote a checkerboard-like structure with system-wide correlations indicating long-range order, consistent with a crystalline-like monolayer.

At 300 K, the IL monolayer still maintains cation–anion alternation, but the directional distribution begins to blur into an increasingly isotropic (i.e., radially symmetric) pattern (see transition region in the middle panel of Fig. 4). Elevated thermal excitations begin to overcome the adhesive forces that anchor ions to specific sites on the hydroxylated sapphire surface, enabling them to hop more frequently between interaction sites while remaining adsorbed at the interface. Peaks in the positional distributions of both cations and anions start to merge, with strong correlations persisting only among the 4 to 5 nearest neighbors. This behavior is consistent with monolayer melting, marked by a gradual transition from discrete rotational symmetry to continuous symmetry, and the emergence of a liquid-like phase. Because the diffusion is still strongly suppressed, but the long-range order is compromised, this is consistent with a commonly observed glassy behavior.

At temperatures of 350 K and above, we observe an isotropic—i.e., direction-independent—distribution of cations and anions around a reference cation, exhibiting continuous rotational symmetry (see bottom panel in Fig. 4). However, faint remnants of the hexagonal structure characteristic of lower temperatures remain visible pointing to short-range order, though these features become increasingly suppressed at 400 K. In parallel, the in-plane correlation length decreases: from 3 to 4 coordination rings at 350 K, to just 2 to 3 visible rings at 400 K. These observations suggest that, even at elevated temperatures, the substrate continues to influence the film structure—although this coupling becomes progressively weaker with increasing thermal energy, consistent with the calculated PMFs (Fig. 3). The structure and the dynamics are consistent with liquid-like behavior.

6. Film morphology and defects

6.1. Establishing the analysis procedure

We want to further quantify the impact that this interplay of interactions on the molecular level has on the topology and morphology of the observed films. However, analyzing the precise shape and structure

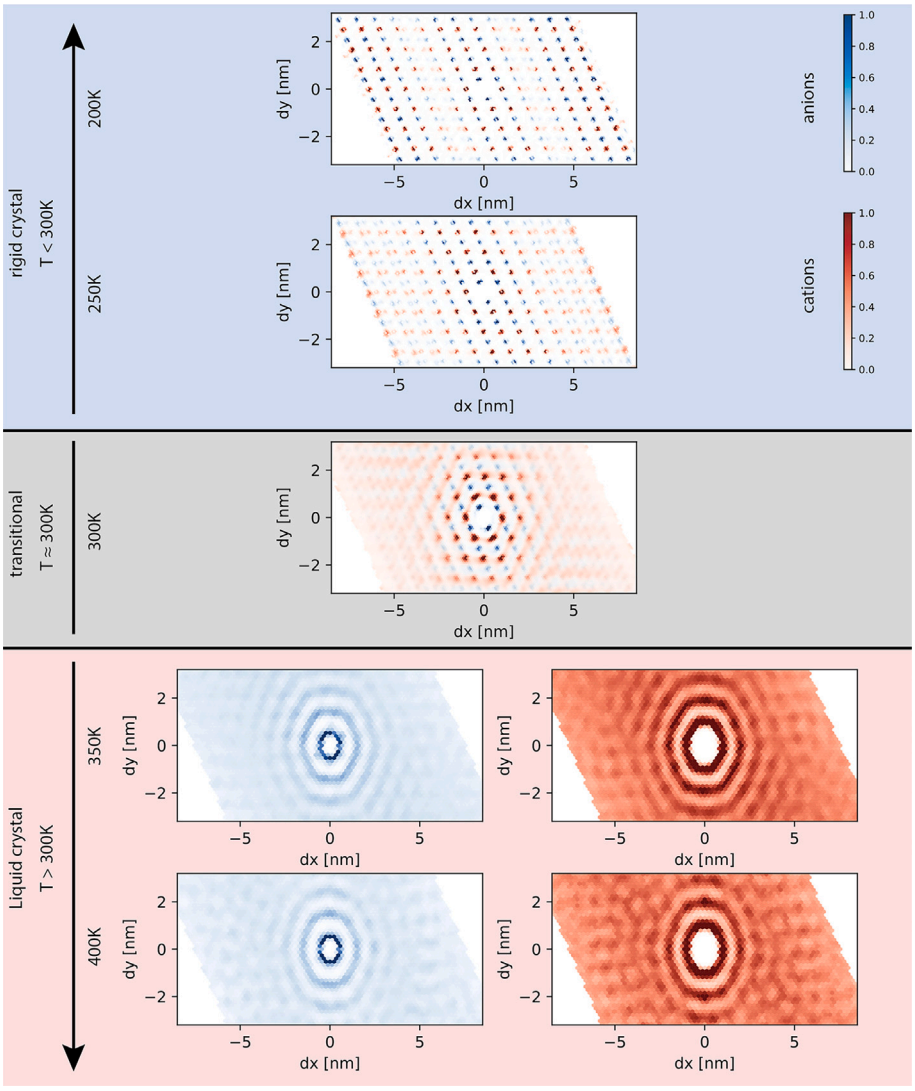

Fig. 4. Relative density distribution functions of monolayer films as a function of temperature. 2Drdfs with respect to a cation in the center at $dx = dy = 0$ are shown for anions (blue) and cations (red). Below the critical temperature threshold (200 K and 250 K, top panel), we observe alternating crystal-like patterns. The distribution is very clearly directionally dependent. The symmetry of this distribution is also closely tied to the symmetry axis of the underlying substrate. The middle panel represents the structure close to the critical temperature (≈300 K) where we observe a glassy-like state between the crystal-like pattern and the direction-independent distribution at higher temperatures. Above the critical temperature (350 K to 400 K, bottom panel), the structure is isotropic, i.e., independent of the direction in the two-dimensional plane and consequently decoupled from the structure of the substrate. The number of oscillations in the density profile also decreases with higher temperatures, indicating a drop in density-density correlation.

of the liquid layer within each frame requires the development of an appropriate tool in which boundaries of the film and defects can be found in trajectories of MD simulations.

The general idea of the tool is to first build a two-dimensional planar graph of the IL molecules in a periodic geometry, where we connect pairs of molecules that find themselves within a threshold distance using custom-made code provided at https://github.com/puls-group/monolayer_analysis and in a ZENODO code archive [36]. Then, we identify the outer edge of the film and the inner boundaries of defects/holes in the film layer (see Fig. 5c for a visualization of a graph representation). Once the boundaries of the IL covering the surface are identified, properties of the film and its defects can be systematically analyzed.

To construct the graph from a snapshot of an IL film, each center of mass (COM) of a molecule is represented by a vertex and added to the graph in the order of its appearance in the trajectory file. For each newly added entry, all pre-existing COMs with a distance less than r_T are determined and an attempt to insert a connecting edge is made. The edge is retained if it does not intersect a previously constructed edge, which keeps the graph planar.

To reduce computational cost and ensure an accurate film topology, we use the 2D radial distribution functions obtained across various temperatures (see Fig. 4) to set the vertex connection threshold to $r_T = 1.3$ nm. This distance includes the first two ion layers, ensuring correct graph construction even without full connectivity. It also allows the detection of internal holes and the separation of disconnected IL regions, which become more common at higher temperatures.

Once all vertices are added to the graph, we construct faces (polygons) in each connected component by starting from an arbitrary vertex and edge. From there, we move to the neighboring vertex and record the direction of arrival. At each new vertex, we sort its outgoing edges by angle and select the next edge in a counter-clockwise direction relative to our entry direction, thus following the face boundary. We repeat this process until we return to the starting vertex and encounter an edge that

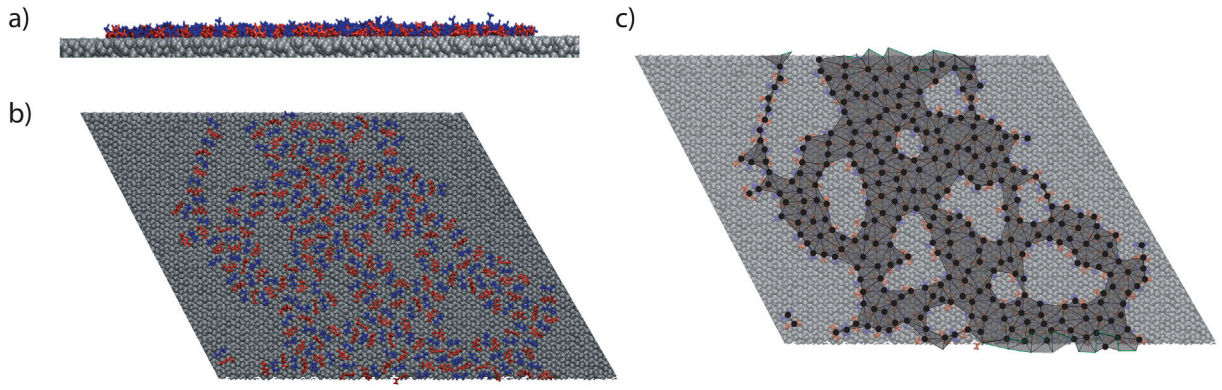

Fig. 5. Graph representation of the monolayer. An example from a system at $T = 400$ K is shown where the supported IL monolayer is shown (a) from the side and (b) from the top. (c) We present the result of the segmentation of the monolayer with the detected covered area being overlaid in dark gray.

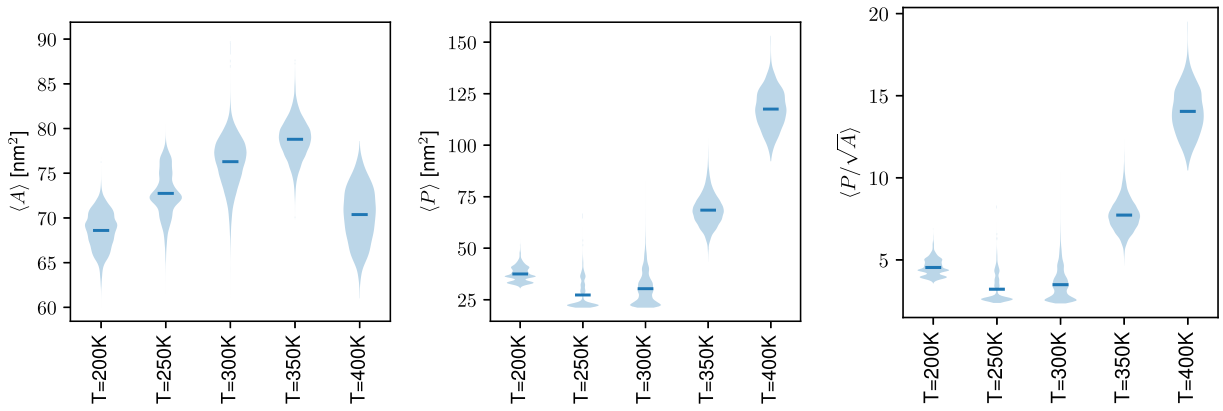

Fig. 6. Statistical analysis of the monolayer film morphology at various temperatures. (Left panel) The mean surface area covered per 100 liquid film ion pairs, and (Middle panel) the associated normalized perimenter. (Right panel) Isoperimetric ratio $P/\sqrt{A}$. (Detailed data about the statistics visualized here provided on ZENODO [37].)

has already been used, completing the face. The finite completion time of this procedure is ensured by the fact that we are traversing a planar graph and following the contour of a face.

Some special cases arise: internal holes are also detected as faces and must be filtered out. We do this based on size, classifying a face as a hole if its outline contains at least $V_{\text{hole}} = 5$ vertices, as appropriate for the current systems. The film's outer boundary also requires special handling. For isolated droplets, the outer edge is traced counter-clockwise, opposite to internal faces, making it easy to identify. However, if the film connects to its periodic copies, the outer edge may not form a closed polygon. In these cases, we track the displacement from the starting point: if the final position differs by a non-zero multiple of the system's period, the detected shape is a strictly periodic polygon and, hence, an outer boundary.

To validate the approach and verify its accuracy, the algorithm was tested on simple geometric configurations, such as regular polygons and planar vertex stripes without periodic boundaries, as well as edge cases such as a single vertex forming a polygon with its periodic images. Visual inspection of selected frames from various systems (e.g., Fig. 5) further confirmed correct behavior. For reproducibility and further use, the full analysis code is publicly available via the referenced GitHub repository and Zenodo archive [36].

6.2. Morphological measures

The construction of the graph allows us to calculate the covered area (A) of the film as the sum of the area of all inner (i.e., clockwise-oriented) faces with fewer than the threshold V_{hole} of vertices, thus leaving out the area of the holes. Similarly, the film perimeter (P) is calculated based on the sum of the perimeters of all outside faces and adding those of all inner faces associated with holes.

All data are normalized to a reference system with 100 ion pairs. As IL ions show no significant conformational changes with temperature, we assume each ion pair occupies approximately the same surface area across systems. Thus, we apply a scaling factor

$$R = \frac{100}{N_{\text{pairs}}}$$

for area-related quantities, including the total number of holes. Length-based measures, such as the perimeter, are scaled by $\sqrt{R}$, consistent with dimensional analysis.

We compute the isoperimetric ratio ($IPR = P/\sqrt{A}$), to quantify how elongated or rugged a film's outline is relative to its area. Lower IPR values suggest a tendency towards compact, circular shapes with higher line tension, while higher values indicate more irregular, finger-like structures and reduced line tension. In non-periodic planar geometry, the minimum IPR is $2\sqrt{\pi}$, achieved by a perfect circle. Polygons always exceed this value, but those with more vertices approximate it more closely (see Fig. 7 for pentagon and hexagon limits). In periodic systems like ours, IPR values can fall below the circular bound due to boundary wrapping, but the trends relating film compactness and the IPR value remain.

To determine the uncertainty of our results, we calculate the mean and the standard deviation σ of each of these properties ($\langle A\rangle$, $\langle P\rangle$, $\langle IPR\rangle$) across all frames within the trajectory upon equilibration.

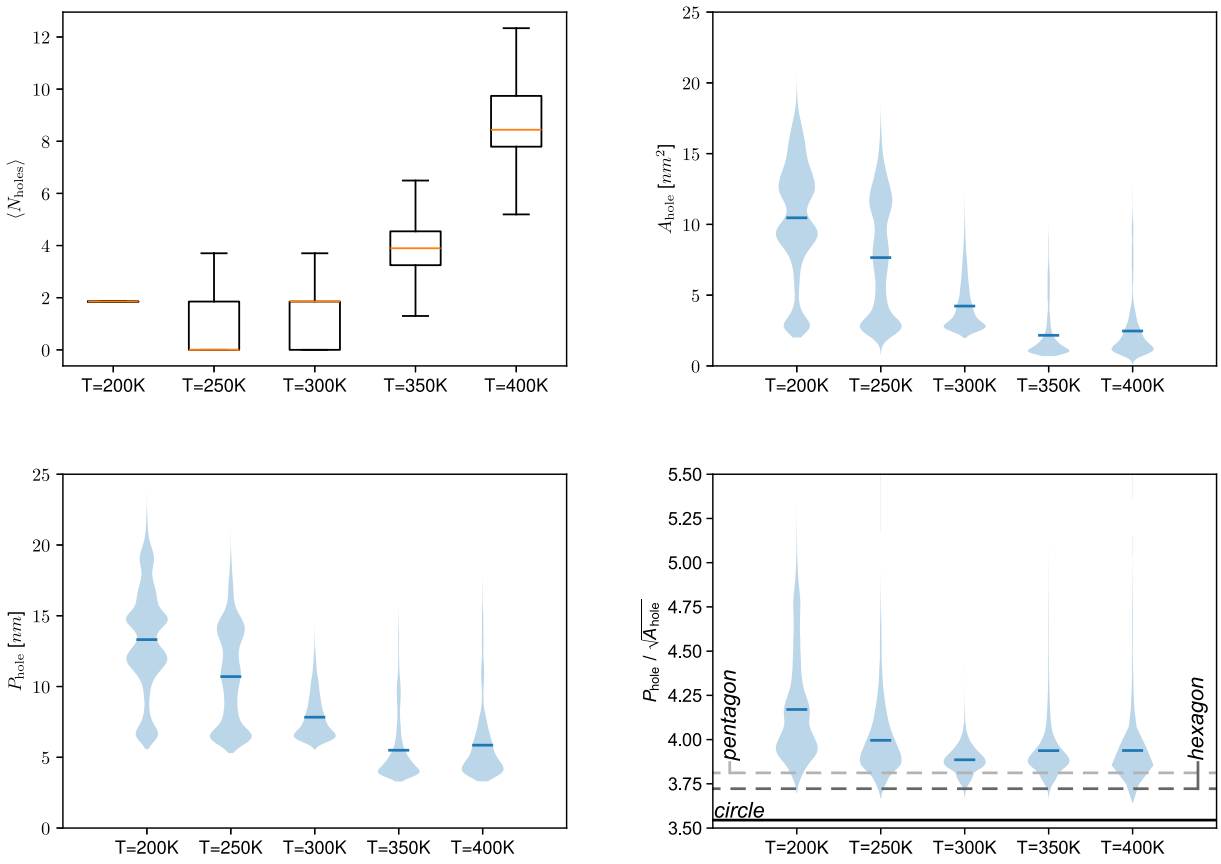

Fig. 7. Morphological analysis of defects. Defects seen as holes in the monolayer films have been identified and characterized in a statistically sound manner using custom-made code provided at https://github.com/puls-group/monolayer_analysis and in the ZENODO code archive [36]. (top left panel) Number of holes as a function of temperature in a box-plot. The mean is represented by the orange line. We see a clear transition in the number of holes with more holes appearing in the liquid state as the temperature rises in line with the criticality observed in Fig. 4. Violin plot representations of the distribution of defect area (top right) and perimeter (bottom left) in monolayer films at various simulation temperatures. (bottom right) The distribution of IPR values of holes in monolayers simulated at between 200 K and 400 K are plotted together with the theoretically minimal IPR values for circles as well as hexagon and pentagon shapes. The raw area and perimeter statistics for holes are available on ZENODO [37].

Finally, we also calculate the standard error $\sigma_{\text{err}} = \sigma/\sqrt{f}$, where f is the number of contributing frames.

6.3. Temperature-dependent morphological properties of the monolayer

With these definitions in place, we examine how various morphological measures evolve with temperature (Fig. 6). As the system transitions from crystalline-like to liquid-like states, the film area A increases due to increased thermal fluctuations. However, this increase remains relatively modest—about 15 %—since ion spacing is largely governed by the distribution of hydroxyl groups on the alumina surface, and individual ions remain bound. As temperature rises, adhesive interactions with the substrate become less dominant relative to increasing entropic contributions, while Coulombic cohesion, already strongly screened, becomes insufficient to maintain order. Consequently, the line tension decreases, leading to a progressive loss of structural integrity of the film.

This behavior is well captured by the changes in the perimeter P of the film. In the crystalline-like regime, the monolayer displays alternating arrays of ions that, through the periodic boundary conditions, stretch infinitely along the (1000) axis. The perimeter P remains nearly constant, constrained by lateral ion interactions, surface anchoring, suppressed diffusion and the fixed number of ions that is incommensurate with completing a full stripe. As the temperature rises into the transition region, increased ion mobility allows the film to relax towards an energetically optimal perimeter-to-area ratio, causing P to decrease. This trend is mirrored in the isoperimetric ratio (IPR), which closely follows P due to minimal changes in A across temperatures.

As the system enters deeper into the liquid-like regime, further reduction in line tension leads to the appearance of voids within the monolayer. Consequently, both P and IPR increase by an order of magnitude. Ultimately, at 400 K, quasi-one-dimensional ion chains and finger-like protrusions begin to form (see Fig. 5b, c), which is reflected in a drop in the film area. This morphological change marks a shift in the balance of forces, as the PMFs suggest (Fig. 3). Cohesive interactions between ions begin to outweigh adhesion to the substrate, while entropic effects become increasingly relevant. Consequently, line tension is significantly reduced, compromising the structural integrity of the film. Nonetheless, the film remains largely connected; detached ion pairs or small islands (see Fig. 5b, c) are rare and typically small.

At even higher temperatures, we expect thermal energy to overcome this constraint as well, leading to the decomposition of the film into isolated ion clusters. However, at this stage the stability of the ions themselves may also be compromised [38].

6.4. Characteristics of defects

Using the graph representation, we can also fully explore the properties of defects within the monolayer, the number of which increases significantly past the transition temperatures (top left panel in Fig. 7). In the crystalline-like phase, defects are large in area A_{hole} and perimeter P_{hole}, because they are associated with long-lived dislocations (top

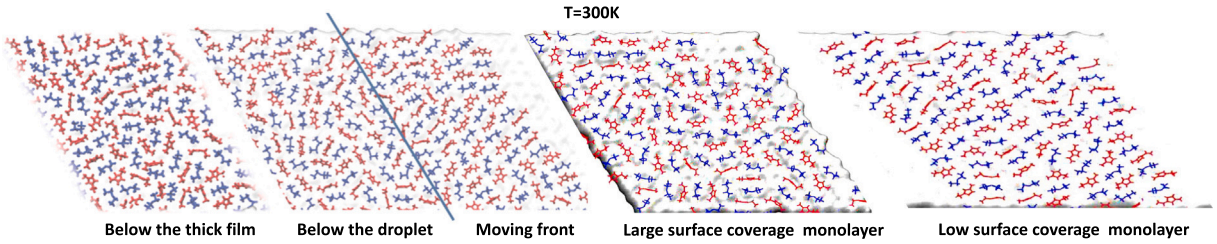

Fig. 8. Effect of confinement on the structure of the film close to the monolayer transition temperature of $T = 300$ K. Short range order is maintained below a thick film, as well as under the droplet and a monolayer at relatively large surface coverage. Long range order is, however, observed in the precursor film during spreading and even more clearly in an unconstrained monolayer, where only the part of the surface with the IL is shown.

right and bottom left panels in Fig. 7). These appear close to the edge of the film when a cooperative diffusive displacement of several ions has taken place. As these motions are rare, such defects also heal very slowly, impacting significantly the statistics.

In the liquid-like state, the defects appear as more frequent holes in the monolayer. On average they are smaller than dislocations at low T, occur more frequently and are often shorter lived. Interestingly, the shape of holes becomes most circular at transition temperatures, as evidenced by a minimum in the IPR and the narrow distribution of values it adopts (bottom right panel in Fig. 7).

In summary, morphological measures associated with the film and the defects show the optimization of shape and structure in the transition region. At lower temperatures, constraints imposed by the substrate restrict self-healing of the film, while at high temperatures the film structure is compromised because of the reduction of the effective potentials among the ions and between the ions and the surface Fig. 5. In the technological context, this provides an interesting opportunity to optimize the operating conditions, especially when the film has a functional role, as in lubricants or in electro-catalysis.

7. The effect of surface saturation

The preceding analysis was conducted under conditions of low surface coverage. As the ionic liquid (IL) surface saturation increases, two structural scenarios become possible:

(i) The system maintains long-range order in the contact layer while forming a second layer on top, thereby gaining cohesion energy from out-of-plane interactions. This behavior has been observed, for example, when the same IL is deposited on gold surfaces, leading to spontaneous bilayer formation, with the second layer adopting an out-of-plane checkerboard structure [5].

(ii) The system retains a monolayer structure to maximize adhesion energy to the substrate, at the expense of increased structural disorder. A similar outcome is observed when the same cation with a chloride anion IL is confined between graphite surfaces, where stronger confinement and packing lead to disordered arrangements [39].

For the current substrate–liquid combination, our findings indicate that the disordered monolayer scenario (ii) prevails. This is supported by the observation that, at the same temperatures, the first layer of a thick IL film solvating the surface of alumina exhibits significantly higher ion density and disorder than the monolayer (first panel in Fig. 8). A similar structure is seen in the contact layer beneath a spreading droplet but not in the protruding film (second panel in Fig. 8). Consistent with these findings, increasing the number of ions within a monolayer relative to the available surface area indeed leads to configurational constraints and greater structural disorder (third panel in Fig. 8). This contrasts with the high degree of order observed at lower saturation (last panel in Fig. 8). Here, the abundance of exposed alumina allows IL ions to maximize the effect of hydrogen bonding with the substrate, fully exploiting the adhesion energy to outweigh the cohesive forces that would otherwise favor bilayer formation.

This analysis underscores the importance of surface coverage and film thickness in determining interface-adjacent structural behavior, with implications for adsorption and diffusive transport in supported IL films. More broadly, it highlights the crucial role of confinement in shifting the location of the region where the transition from crystal-like to the liquid-like behavior takes place in such systems.

8. Discussion

One of the hallmarks of ionic liquids is their lack of true long-range crystalline order, even at low temperatures, when they become glassy. By contrast, monolayers can exhibit crystalline order when ions' shape and the positioning of their moieties that favor strong adhesive interactions are geometrically commensurate with the lattice of the solid. Because it dominates, adhesion may hinder configurations optimal for cohesion, but together, at low temperatures, the two strongly suppress diffusion and promote long range order. In the current system, adhesiveness stems from stable hydrogen bonds, though other interaction types can have the same effect [6]. Conversely, weakly interacting cations with longer alkyl chains may tend to inhibit crystallization.

As temperature increases, substrate-induced crystalline order is progressively but inevitably lost, and long-range order gradually disappears. If in the process adhesive interactions become less significant relative to cohesive ones (for example, hydrogen bonds being less stable than ionic interactions), a glassy state may form, in which cohesive forces, and hence film density, are optimized, while diffusion remains strongly suppressed. At even higher temperatures, cohesive forces become insufficient to maintain correlations beyond nearest neighbors, and ions become highly mobile, as expected in a liquid-like environment. At low surface coverage, this can compromise film integrity.

A standard way to form the glassy state, however, is by cooling liquids down from high temperatures. Stabilized by adhesion, glassy monolayers and thin IL films are then expected to appear at temperatures where the bulk IL remains liquid [3]. However, further cooling alone may not suffice to reach the crystalline state due to slow diffusion and quenched disorder. This likely explains why glassy states are commonly observed in a variety of systems [40–44].

An interesting interplay between adhesive and cohesive interactions occurs when the surface is saturated, and multilayered structures appear [45,46]. Adhesion between the IL and the substrate is in direct competition with the interactions between IL layers, hence the transitions between crystalline, glassy and liquid structures are shifted. Moreover, order in the contact layer will promote structuring of higher layers [6,13], but in turn, interactions between the layers will support some disorder in the contact layer, as does the entropic contribution to the free energy growing with temperature.

9. Conclusions

In this manuscript, we employed molecular dynamics simulations to investigate the structural and morphological properties of $[C_2Mim][NTF_2]$ monolayer films that spontaneously form on a neutral, hydroxylated alumina substrate. To study the structure, the

dynamics and the defects in the monolayer, we developed a graph-based analysis tool. With the code freely available, this tool can be utilized not only in the context of simulations but can also be applied to high-resolution imaging data from experiments.

Our study reveals two distinct regimes in the behavior of these liquid films: At low temperatures, the films exhibit crystalline-like order with few defects, driven by the strong coupling between nearly immobile ions and the underlying crystal lattice of the substrate. In contrast, at higher temperatures, the films display dynamic, liquid-like behavior, characterized by a high likelihood of small, short-lived defects—particularly under conditions of low surface coverage. During the transition between these regimes, the film adopts an optimal area-to-circumference ratio, governed by the balance between substantial line tension at the film edge and sufficient ion mobility to heal emerging defects.

In a more general context, our results highlight the key factors that determine the structure and stability of supported IL films:

(i) adhesive forces and the specific interactions between the IL and the functional groups on the substrate,
(ii) lateral cohesive Coulomb interactions, which drive the formation of alternating anion–cation patterns at the interface,
(iii) out-of-plane cohesive forces between layers, which diminish the relative importance of adhesion to the substrate once the surface is fully covered, and
(iv) entropic contributions that enhance ion diffusion both on the surface and between layers.

Taken together, these insights deepen our understanding of the interplay between temperature, surface coverage, adhesive and inter-ionic forces in determining the structural organization of ionic liquid films, which continuously changes from a crystalline-like to liquid-like with temperature. They provide a foundation for rational design of supported IL layers in applications ranging from catalysis to electrochemical devices, where controlling film morphology is crucial for performance.

CRediT authorship contribution statement

Kevin Höllring: Writing – original draft, Visualization, Software, Methodology, Investigation, Formal analysis, Data curation, Conceptualization. **Nataša Vučemilović-Alagić:** Visualization, Formal analysis. **David M. Smith:** Supervision. **Ana-Sunčana Smith:** Writing – review & editing, Resources, Project administration, Investigation, Funding acquisition, Data curation, Conceptualization.

Declaration of competing interest

The authors declare that they have no known competing financial interests or personal relationships that could have appeared to influence the work reported in this paper.

Acknowledgements

We acknowledge funding by the Deutsche Forschungsgemeinschaft (DFG, German Research Foundation) – Project-ID 416229255 – SFB 1411 Particle Design and Project-ID 431791331 - SFB 1452 Catalysis at Liquid Interfaces (CLINT) for support. The authors gratefully acknowledge the scientific support and HPC resources provided by the Erlangen National High Performance Computing Center (NHR@FAU) of the Friedrich Alexander Universität Erlangen - Nürnberg (FAU) and University of Zagreb Computing Centre - SRCE.

Data availability

The data have been published in a Zenodo archive and the code has been made available on GitHub. Further data are made available upon request.

References

[1] A. Riisager, R. Fehrmann, M. Haumann, P. Wasserscheid, Eur. J. Inorg. Chem. 2006 (2006) 695–706.
[2] N. Vučemilović-Alagić, R.D. Banhatti, R. Stepić, C.R. Wick, D. Berger, M.U. Gaimann, A. Baer, J. Harting, D.M. Smith, A.-S. Smith, J. Colloid Interface Sci. 553 (2019) 350–363.
[3] K. Höllring, A. Baer, N. Vučemilović-Alagić, D.M. Smith, A.-S. Smith, J. Colloid Interface Sci. 657 (2024) 272–289.
[4] K.T. Höllring, Multi-Scale Coupling in Selected Soft and Living Matter Systems, Friedrich-Alexander-Universitaet Erlangen-Nuernberg (Germany), 2024.
[5] M. Meusel, M. Lexow, A. Gezmis, A. Bayer, F. Maier, H.-P. Steinrück, Langmuir 36 (2020) 13670–13681.
[6] M. Meusel, M. Lexow, A. Gezmis, S. Schötz, M. Wagner, A. Bayer, F. Maier, H.-P. Steinrück, ACS Nano 14 (2020) 9000–9010.
[7] F. Krebs, O. Höfft, F. Endres, Coatings 13 (2023) 1182.
[8] S.A. Rastabi, G. Razaz, M. Hummelgård, T. Carlberg, N. Blomquist, J. Örtegren, H. Olin, J. Power Sources 523 (2022) 231066.
[9] Y.-K. Ahn, J. Park, D. Shin, S. Cho, S.Y. Park, H. Kim, Y. Piao, J. Yoo, Y.S. Kim, J. Mater. Chem. A 3 (2015) 10715–10719.
[10] J.J. Segura, A. Elbourne, E.J. Wanless, G.G. Warr, K. Voïtchovsky, R. Atkin, Phys. Chem. Chem. Phys. 15 (2013) 3320–3328.
[11] R. Lhermerout, C. Diederichs, S. Perkin, Lubricants 6 (2018) 9.
[12] A.A. Lee, C.S. Perez-Martinez, A.M. Smith, S. Perkin, Phys. Rev. Lett. 119 (2017) 026002.
[13] Z. Brkljača, M. Klimczak, Z. Milicevic, M. Weisser, N. Taccardi, P. Wasserscheid, D.M. Smith, A. Magerl, A.-S. Smith, J. Phys. Chem. Lett. 6 (2015) 549–555.
[14] R. Horn, D. Evans, B. Ninham, J. Phys. Chem. 92 (1988) 3531–3537.
[15] R. Atkin, G.G. Warr, J. Phys. Chem. C 111 (2007) 5162–5168.
[16] M. Lexow, F. Maier, H.-P. Steinrück, Adv. Phys. X 5 (1) (2020) 1761266.
[17] H.-P. Steinrueck, P. Wasserscheid, Catal. Lett. 145 (2015) 380–397.
[18] M.J. Earle, J.M. Esperança, M.A. Gilea, J.N.C. Lopes, L.P. Rebelo, J.W. Magee, K.R. Seddon, J.A. Widegren, Nature 439 (2006) 831–834.
[19] T. Cremer, M. Killian, J.M. Gottfried, N. Paape, P. Wasserscheid, F. Maier, H.-P. Steinrück, ChemPhysChem 9 (2008) 2185–2190.
[20] R. Souda, J. Phys. Chem. B 112 (2008) 15349–15354.
[21] D. Van Der Spoel, E. Lindahl, B. Hess, G. Groenhof, A.E. Mark, H.J. Berendsen, J. Comput. Chem. 26 (2005) 1701–1718.
[22] J.N.C. Lopes, J. Deschamps, A.A.H. Pádua, J. Phys. Chem. B 108 (2004) 2038–2047.
[23] M.S. Kelkar, E.J. Maginn, J. Phys. Chem. B 111 (2007) 4867–4876.
[24] N. Vučemilović-Alagić, Computational study of the physical and interfacial properties of imidazolium-based ionic liquids, (Ph.D. thesis), Friedrich-Alexander-Universität Erlangen-Nürnberg (Germany), 2021.
[25] W.D. Cornell, P. Cieplak, C.I. Bayly, P.A. Kollman, J. Am. Chem. Soc. 115 (1993) 9620–9631.
[26] R.T. Cygan, J.-J. Liang, A.G. Kalinichev, J. Phys. Chem. B 108 (2004) 1255–1266.
[27] J.D. Gale, A.L. Rohl, Mol. Simul. 29 (2003) 291–341.
[28] R. Burt, G. Birkett, M. Salanne, X.S. Zhao, J. Phys. Chem. C 120 (2016) 5244–15250.
[29] S. Malali, M. Foroutan, J. Phys. Chem. C 121 (21) (2017) 11226–11233.
[30] Y. Guan, Q. Shao, W. Chen, S. Liu, X. Zhang, Y. Deng, J. Phys. Chem. C 121 (42) (2017) 23716–23726.
[31] N. Ojaghlou, D. Bratko, M. Salanne, M. Shafiei, A. Luzar, ACS Nano 14 (7) (2020) 7987–7998.
[32] P.-G. De Gennes, Rev. Mod. Phys. 57 (3) (1985) 827.
[33] S. Zhang, Y. Lu, C. Peng, H. Liu, D.-E. Jiang, J. Phys. Chem. C, 123 (1) (2018) 618–624.
[34] S. Kumar, J.M. Rosenberg, D. Bouzida, R.H. Swendsen, P.A. Kollman, J. Comput. Chem. 13 (8) (1992) 1011–1021.
[35] S. Kumar, J.M. Rosenberg, D. Bouzida, R.H. Swendsen, P.A. Kollman, J. Comput. Chem. 16 (11) (1995) 1339–1350.
[36] K. Höllring, N. Vučemilović-Alagić, D.M. Smith, A.-S. Smith, Struct. Topol. (2024) https://doi.org/10.5281/zenodo.10707053
[37] K. Höllring, N. Vučemilović-Alagić, D.M. Smith, A.-S. Smith, Dataset: Criticality In An Imidazolium Ionic Liquid Fully Wetting a Sapphire Support (2024) https://doi.org/10.5281/zenodo.10706965
[38] F. Heym, B.J. Etzold, C. Kern, A. Jess, Green Chem. 13 (6) (2011) 1453–1466.
[39] M. Sha, G. Wu, H. Fang, G. Zhu, Y. Liu, J. Phys. Chem. C 112 (47) (2008) 18584–18587.
[40] B. Wang, L. Li, Langmuir 37 (2021) 14753–14759.
[41] X. Gong, A. Kozbial, L. Li, Chem. Sci. 6 (6) (2015) 3478–3482.
[42] R. An, X. Qiu, F.U. Shah, K. Riehemann, H. Fuchs, Phys. Chem. Chem. Phys. 22 (26) (2020) 14941–14952.
[43] X. Gong, A. Kozbial, L. Li, ACS Appl. Mater. Interfaces 7 (13) (2015) 7078–7081.
[44] T. Kobayashi, J. Smiatek, M. Fyta, Phys. Chem. Chem. Phys. 24 (27) (2022) 25411–25419.
[45] R. An, L. Huang, Y. Long, B. Kalanyan, X. Lu, K.E. Gubbins, Langmuir 32 (3) (2016) 743–750.
[46] R. An, M. Wu, J. Li, X. Qiu, F.U. Shah, J. Li, Phys. Chem. Chem. Phys. 21 (48) (2019) 26387–26398.